Applied Surface Science 644 (2024) 158748

Contents lists available at ScienceDirect

Applied Surface Science

journal homepage: www.elsevier.com/locate/apsusc

Full Length Article

Substrate-tuned dielectric screening effect on optical properties of monolayer $MoSe_2$

Liusheng Huang [a,b], Honggang Gu [a,c,d,*], Mingsheng Fang [a], Shiyuan Liu [a,b,c,*]

[a] State Key Laboratory of Intelligent Manufacturing Equipment and Technology, Huazhong University of Science and Technology, Wuhan, Hubei 430074, China
[b] School of Optical and Electronic Information, Huazhong University of Science and Technology, Wuhan, Hubei 430074, China
[c] Optics Valley Laboratory, Hubei 430074, China
[d] Guangdong HUST Industrial Technology Research Institute, Guangdong Provincial Key Laboratory of Manufacturing Equipment Digitization, Dongguan, Guangdong 523003, China

ARTICLE INFO

Keywords:
Monolayer $MoSe_2$
Substrate effect
Dielectric screening effect
Critical point analysis
Spectroscopic ellipsometry

ABSTRACT

Grasping the intricate mechanisms for the influences of dielectric screening from diverse substrates on the optical properties of ultra-thin two-dimensional materials is crucial for related device design. This study investigates the substrate impacts on the optical properties of monolayer $MoSe_2$ by combining the spectroscopic ellipsometry (SE) and first-principle calculations. Featured absorption peaks of monolayer $MoSe_2$ on substrates of quartz, silicon, and sapphire are meticulously analyzed via critical point (CP) analysis on the dielectric functions determined by SE. Results indicate that variation in substrates induces notable shifts in energy positions of the absorption peaks due to different dielectric screening effects. The study further uncovers electron transfer from silicon substrate to monolayer $MoSe_2$, leading to alterations in the band structure. By integrating CP analysis with first-principle calculations, we gain a comprehensive understanding of the optical transitions corresponding to CPs in the monolayer $MoSe_2$ on various substrates. This establishes that the energy shifts of CPs regulated by substrate-induced dielectric screening are highly correlated with the positions of their corresponding optical transitions in momentum space. These findings underscore the pivotal role of substrate selection in customizing the optical properties of two-dimensional materials, providing valuable insights for the design and optimization of $MoSe_2$-based photonic devices.

1. Introduction

Over the past two decades, the emergence of two-dimensional (2D) materials has revolutionized the landscape of material science, offering a powerful platform for the development of novel optoelectronics devices with unprecedented performances[1–4]. Transition metal dichalcogenides (TMDCs), a representative class of 2D materials with layered MX_2 structures, have attracted significant attentions due to their unique electronic and optical properties, such as tunable bandgap, pronounced optical anisotropy, high electron mobility, enormous excitonic binding energies, and exciton hall effect[5–9]. Moreover, as the thickness of TMDCs progressively diminishes to a monolayer level, a host of novel physical phenomena are observed in comparison to their bulk counterparts. Examples include the enhancement of exciton (electron-hole pair) binding energy[10], the transition of the band structure from an indirect to a direct bandgap[11], and the substantial amplification of photoluminescence (PL)[12], among others. For monolayer TMDC materials, due to their atomically thin nature, the electric field lines between electron-hole pairs extend into low dielectric environments (such as air), resulting in a significantly reduced dielectric screening effect compared to bulk materials[13]. This phenomenon further leads to an enhancement of long-range Coulomb interactions between electron-hole pairs, which in turn significantly renormalizes the quasiparticle band structure and increases the exciton binding energy[14]. Under these circumstances, the dielectric environments provided by different substrates have a non-negligible impact on the dielectric screening effect of monolayer TMDC materials. However, compared to the modulation of exciton binding energy by different substrates, the optical properties of monolayer TMDCs are relatively less influenced by substrate effects. Conventional characterization techniques, such as absorption, PL,

* Corresponding authors at: State Key Laboratory of Intelligent Manufacturing Equipment and Technology, Huazhong University of Science and Technology, 1037 Luoyu Road, Wuhan, Hubei 430074, China.
E-mail addresses: hongganggu@hust.edu.cn (H. Gu), shyliu@hust.edu.cn (S. Liu).

https://doi.org/10.1016/j.apsusc.2023.158748
Received 20 July 2023; Received in revised form 7 October 2023; Accepted 24 October 2023
Available online 26 October 2023

scanning tunneling spectroscopy, Raman spectroscopy, etc., struggle to accurately obtain the dielectric functions of monolayer TMDCs under different substrates, making it difficult to reveal the underlying regulatory mechanisms of substrate effects. Therefore, it is of paramount importance to develop an accurate and comprehensive method to characterize the influence of substrate screening effect on the optoelectronic properties of monolayer TMDCs for future device applications.

Among TMDCs, the monolayer molybdenum diselenide ($MoSe_2$) has garnered widespread attention due to its exceptional optoelectronic properties[15–17]. Distinct from the octahedral structure, the monolayer 2H-phase $MoSe_2$ features a trigonal prismatic coordination, with a direct bandgap of up to 1.6 eV[18,19]. Moreover, the band splitting induced by spin–orbit coupling in monolayer 2H-phase $MoSe_2$ reaches 180 meV, which is greater than 149 meV observed in monolayer 2H-phase MoS_2[20]. In comparison to multilayer structures, the PL intensity of monolayer 2H-phase $MoSe_2$ is significantly enhanced, with the PL peak position at approximately 1.55 eV[21]. The average carrier mobility can reach 50 $cm^2/V{\cdot}s$, with a high on/off current ratio exceeding 10^6[22]. These unique characteristics endow the monolayer 2H $MoSe_2$ with extensive application potential in various fields, such as solar cells, photodetectors, spintronic devices, and field-effect transistors[20,22–24]. To better optimize the design of $MoSe_2$-based optoelectronic devices, it is crucial to obtain accurate and quantitative optical properties of monolayer 2H $MoSe_2$ under different dielectric environments provided by various substrates, and to reveal the underlying mechanisms of substrate effects on its optical properties.

In recent years, researches on the influence of substrate screening effects on the optoelectronic properties of 2D materials have been growing[25–30]. Ugeda *et al.* investigated the significant renormalization of the quasiparticle band of monolayer $MoSe_2$ by the substrate through the scanning tunneling microscopy and theoretical calculations [25]. Qiu *et al.* calculated the renormalization of the quasiparticle band and spectra of few-layer black phosphorus due to the substrate dielectric screening effect[26]. Drüppel *et al.* reported that theoretical calculations confirmed a weak redshift of the absorption exciton peak of monolayer MoS_2 as the substrate dielectric constant increases[27]. Borghardt *et al.* reported a redshift of the PL exciton peak in monolayer TMDCs as the dielectric environment rises[28]. However, as stated above, the experimental techniques adopted in these studies struggle to directly measure the accurate dielectric functions of monolayer TMDCs, and it is difficult to quantitatively study the subtle impact of substrate screening effects on the optical properties. Consequently, research on accurately characterizing the influence of substrate screening effects on the broadband dielectric functions of monolayer $MoSe_2$ remains scarce. However, SE has emerged as a robust and reliable tool for the meticulous characterization of dielectric properties in nanomaterials. Prior research evidences the wide-ranging applicability of SE in ascertaining the dielectric function of 2D materials with elevated accuracy[31–35].

In this work, we conduct an exhaustive exploration of the optical properties of monolayer $MoSe_2$ under the influences of different substrates including the quartz, silicon, and sapphire. Spectroscopic ellipsometry (SE) is employed to acquire the dielectric function of monolayer 2H-$MoSe_2$ on different substrates over the energy range of 1.24–4.76 eV at room temperature. Utilizing a fusion of critical point (CP) analysis and first-principle calculations, we comprehensively unravel the intricate details of optical transitions at six distinct CPs (A-F), thereby ascertaining the intricate influence of substrate-induced dielectric screening on the optical properties of monolayer $MoSe_2$. We discern that the CP energy positions of monolayer $MoSe_2$ undergo observable shifts attributable to an enhanced dielectric screening effect stemming from the increase in the dielectric constant of the substrate. Most notably, CPs A and B experience a substantial redshift up to 10.3 meV and 9.7 meV, respectively. In our study, we've identified distinct behaviors of CPs based on their location in momentum space. Specifically, CPs A, B, and F, which are associated with optical transitions at the K-point, consistently undergo redshifts with increasing substrate dielectric constant across all substrates. On the other hand, CPs C, D, and E, linked to transitions outside the K-point, exhibit blueshifts on transparent insulating substrates like sapphire and quartz. This suggests that the exciton binding energy E_b of monolayer $MoSe_2$ might be more sensitive to dielectric changes on these substrates. However, the situation on the silicon substrate is more intricate. We've observed potential charge transfer between the silicon substrate and $MoSe_2$, leading to alterations in the band structure. This interplay is likely the reason behind the absence of CP D and the pronounced redshift of CPs C and E on silicon, compared to their behavior on quartz and sapphire substrates. Our findings furnish pivotal insights into the substrate-dependent optical behavior of the monolayer $MoSe_2$, which will promote more comprehensive understanding and precise control of its optical characteristics for potential applications.

2. Experiments

2.1. Sample preparation and characterization

The monocrystal monolayer 2H-$MoSe_2$ triangular grains on substrates of quartz, silicon, and sapphire were provided by SixCarbon Technology Shenzhen. These grains, with sizes reaching up to 70 μm, are grown on an Al_2O_3 (sapphire) substrate through the chemical vapor deposition (CVD) process. The samples on the sapphire substrate are then transferred to quartz and silicon substrates using the PMMA (Polymethyl Methacrylate) method. The quality of the triangular grains is confirmed through Raman spectroscopy and PL spectra, measured by a commercial micro-Raman equipment (Horiba iHR550) at an excitation wavelength of 532 nm. The surface conditions and thicknesses of 2H-$MoSe_2$ triangular grains are inspected by using the Scanning Electron Microscope (SEM) (FEI QUANTA 200) and Atomic Force Microscope (AFM) (STM-1000), respectively. Elemental composition analysis of monolayer 2H-$MoSe_2$ on quartz, silicon, and sapphire substrates is facilitated using the X-ray photoelectron spectrometer (Kratos AXIS Supra+) for X-ray photoelectron spectroscopy (XPS) acquisition.

2.2. Ellipsometry measurements

A customized ultra-micro-spot spectroscopic ellipsometer, developed in collaboration with Wuhan Eoptics Technology Co., was employed to study the monocrystal monolayer 2H-$MoSe_2$ triangular samples on substrates of quartz, silicon, and sapphire at room temperature. Through meticulous geometry optimization, the elliptical light spot of the ellipsometer achieves a short axis of approximately 30 μm and a long axis of approximately 60 μm at a fixed angle of 60°. The micro-probe system is a specifically designed triplet compound achromatic lens with specifications including an outer diameter of 13 mm, a focal length of 30 mm, a back focal length of 25 mm, and a numerical aperture (NA) of 0.22, the system is also carefully calibrated to ensure the measurement accuracy. This setup ensures that the probing spot size is smaller than the sample size of 70 μm, making it suitable for inspecting the monocrystal monolayer 2H-$MoSe_2$ grains. Additionally, a CCD camera is installed directly above the sample stage of the ellipsometer to assist in identifying the exact location of the ultra-micro spot on the sample. SE measurements were carried out covering an energy range of 1.24–4.76 eV.

2.3. Density functional theory (DFT) calculations

To construct the hexagonal unit cell of $MoSe_2$, we employed the experimentally measured lattice constants, namely $a = b = 3.288$ Å and $c = 12.9$ Å [36]. All calculations were performed using the Vienna Ab initio Simulation Package (VASP v5.4.4)[37]. In these calculations, we opted for the generalized gradient approximation of the Perdew-Burke-Ernzerhof (PBE) functional based on the projected augmented wave

(PAW) pseudopotentials to describe the exchange–correlation potential. For the model of monolayer $MoSe_2$, a vacuum layer of 20 Å was utilized to eliminate interactions between adjacent units, and the DFT-D2 method of Grimme was applied to correct for Van der Waals interactions[38]. During the process of geometrical optimization, the structure was optimized using the PBE functional based on PAW pseudopotentials with an energy cutoff of 600 eV, and a 12 × 12 × 1 k-point mesh centered at Γ was employed for Brillouin zone sampling. We established convergence criteria of 0.01 eV/Å for force and 10^{-5} eV for total energy. When calculating band structures and projected density of states (PDOS), we continued to use the PBE functional based on PAW pseudopotentials with an energy cutoff of 600 eV, while a denser 15 × 15 × 1 k-point mesh centered at Γ was employed for Brillouin zone sampling, and an electronic convergence criterion of 10^{-8} was set to ensure calculation accuracy. The effect of spin–orbit coupling (SOC) was considered in all calculations.

3. Results and discussion

2H-phase $MoSe_2$ has a hexagonal crystal system and belongs to the $P6_3/mmc$ space group (lattice constants a = b = 3.288 Å, c = 12.9 Å) [36]. As shown in the inset of Fig. 1(a), the crystal structure of monolayer 2H-phase $MoSe_2$ consists of two layers of Se atoms distributed on opposite surfaces, with one layer of Mo atoms sandwiched in between, forming a sandwich-like structure. Fig. 1(a) displays the Raman spectrum of CVD-grown monocrystal monolayer 2H-$MoSe_2$ on sapphire substrate, where a prominent out-of-plane vibrational phonon mode A_{1g} can be observed at 241.6 cm^{-1}. According to previous reports, the A_{1g} peak of $MoSe_2$ experiences a redshift as the thickness decreases due to the diminishing influence of interlayer coupling on the electron–phonon interaction [21,39–41]. The position at 241.6 cm^{-1} is consistent with previous reports[21,39,40], indicating that the CVD-prepared monocrystal monolayer 2H-$MoSe_2$ sample has high purity and a monolayer structure. Fig. 1(b) presents the PL spectrum, indicating a significant emission peak at around 1.55 eV for CVD-grown monocrystal monolayer 2H-$MoSe_2$ on the sapphire substrate. This is in agreement with the direct bandgap 1.6 eV of monolayer 2H-phase $MoSe_2$ and consistent with previous research findings[17,25,42,43]. Moreover, the relatively narrow full width at half maximum (FWHM) of 54 meV for the PL peak further confirms the high quality of the prepared sample[41]. The Raman and PL characterizations of samples on the quartz substrate, depicted in Supplementary Material Fig. S1 (a, b), indicate that the samples transferred from the sapphire to the quartz substrate maintain equivalent superior performance. This study refrains from extensive examination of the samples on the silicon substrate due to the negligible intensity of their Raman and PL signals. Supplementary Material Fig. S2 (a-f) presents the XPS profiles and corresponding orbital fitting outcomes for monolayer 2H-$MoSe_2$ on substrates of sapphire, quartz, and silicon. These findings, closely aligned with preceding reports, underscore the ultra-high purity of monolayer 2H-$MoSe_2$ across different substrates[22,44]. Additionally, as shown in Fig. 2(c), the AFM image of CVD-grown monocrystal monolayer 2H-$MoSe_2$ on the sapphire substrate exhibits a triangular grain morphology. Through AFM height analysis, we determined that the thickness of the sample is approximately 0.75 nm, again suggesting a monolayer structure, which is consistent with previous values[17,22,44]. Fig. 1(d) exhibits the SEM image of monocrystal monolayer 2H-$MoSe_2$ on the silicon substrate, clearly revealing a standard triangular morphology with high crystal surface quality. Moreover, the image demonstrates that the maximum grain size of the sample reaches 70 μm, which is larger than the 50 μm diameter micron light spot required for ellipsometry testing, thus ensuring the quality of ellipsometric measurements. These characterization results collectively

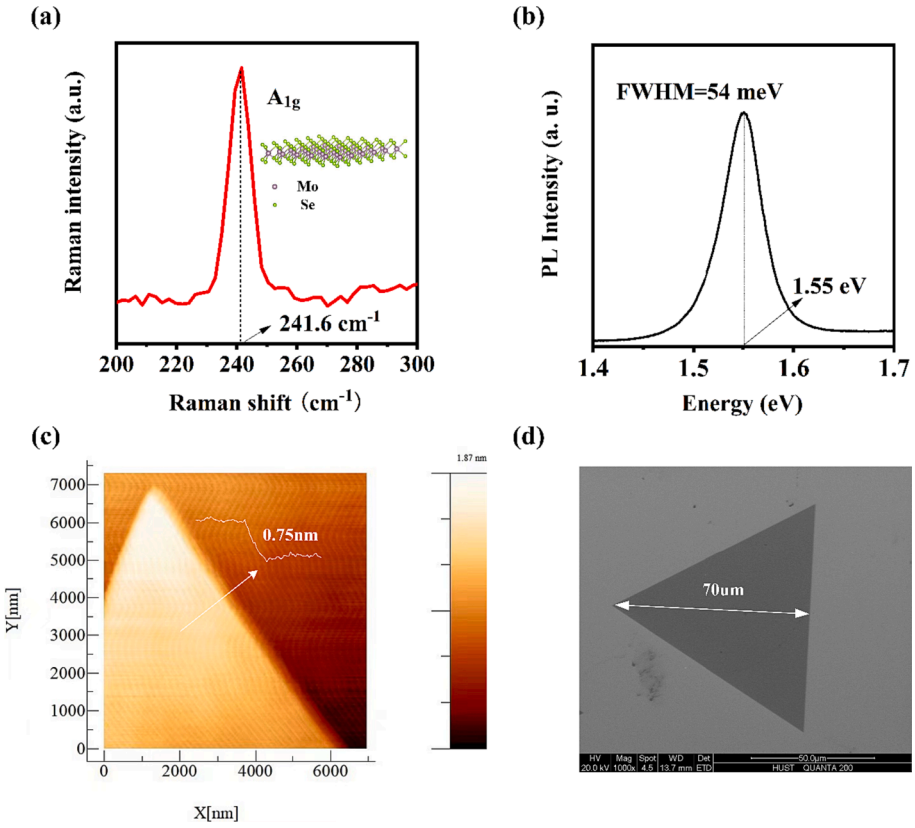

Fig. 1. Characterization results of CVD-grown monocrystal monolayer 2H-phase $MoSe_2$: (a) Raman spectrum of monolayer $MoSe_2$ on sapphire substrate, with the inset showing the crystal structure of monolayer 2H $MoSe_2$; (b) PL spectrum of monolayer $MoSe_2$ on sapphire substrate; (c) AFM image of monolayer $MoSe_2$ on sapphire substrate, with the inset displaying the height profile indicated by the white arrow; (d) SEM image of monolayer $MoSe_2$ on silicon substrate, showing that the grain size can reach up to 70 μm.

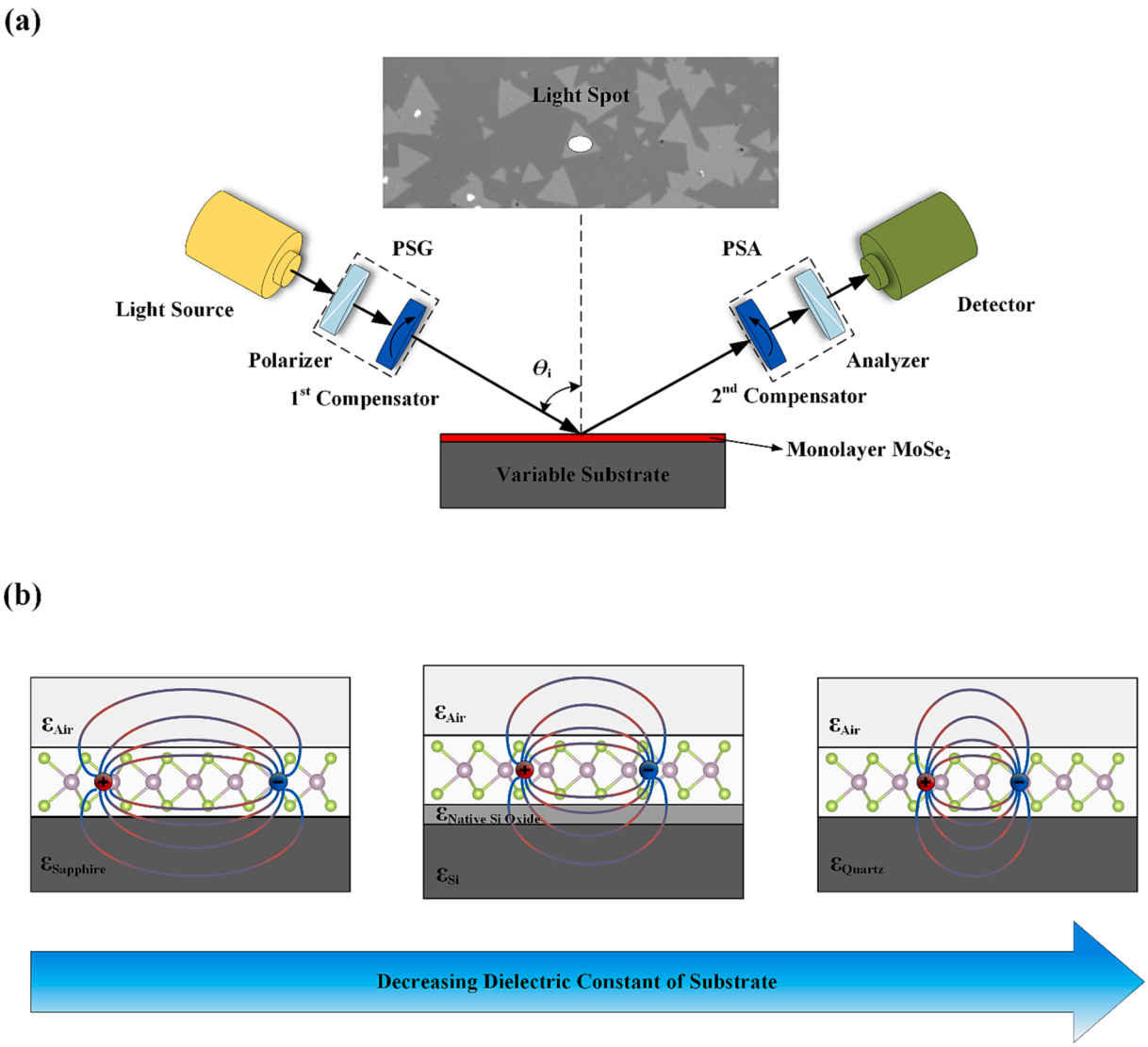

Fig. 2. (a) Schematic of the ultra-micro-spot spectroscopic ellipsometer based on double-rotating compensator principle used in this study, with the inset showing the CCD image of the light spot irradiated on the sample surface in the SE measurement; (b) Optical models of monolayer 2H $MoSe_2$ samples on substrates of sapphire, silicon, and quartz, demonstrating that the dielectric screening effect of monolayer $MoSe_2$ decreases as the substrate dielectric constant decreases.

confirm the extremely high qualities of the monocrystal monolayer 2H-$MoSe_2$ samples under test, providing a solid foundation for the reliability of subsequent SE test and analysis.

Fig. 2(a) presents a schematic of the ultra-micro-spot spectroscopic ellipsometer based dual-rotating compensator principle to investigate the optical properties of monocrystal monolayer 2H $MoSe_2$ on different substrates. As a widely applied characterization technique for nano-materials and nanofilms, the SE operates on the principle of detecting and analyzing the polarization state change of the polarized light after interacting with the sample, thus enabling a comprehensive analysis of the sample including both of the optical properties and geometrical profiles[32,33,45]. As shown in Fig. 2(a), the polarization state of the light changes after passing through the sample, and these changes can be utilized to further obtain the sample's dielectric functions and other related information. In order to characterize the polarization state changes, a pair of ellipsometric parameters (Ψ, Δ) can generally be used for description. Here, tan(Ψ) and Δ represent the amplitude ratio and phase difference between the p-polarized light and s-polarized light, respectively. The ellipsometric parameters can be obtained from the reflection coefficients of the p-polarized light (r_p) and s-polarized light (r_s), as given by

$$\rho = r_p/r_s = \tan(\Psi)\cdot e^{i\Delta} \quad (1)$$

where ρ represents the ellipsometric ratio. Fig. 2(a) illustrates the image captured by the CCD used for assisting spot positioning, indicating the position of the light spot on the sample during the SE measurement process. In this study, we conducted SE measurements on monocrystal monolayer 2H-phase $MoSe_2$ on different substrates with an incidence angle of $\theta = 60^\circ$ covering an energy range of 1.24–4.76 eV.

The SE is a model-based technique, and the SE analysis requires to construct an proper optical model to fit the measured ellipsometric spectra, in which the dielectric functions of monolayer $MoSe_2$ are described parametrically using oscillators model[32]. Finally, based on the constructed optical and dielectric models, theoretical ellipsometric parameters are calculated using the transfer matrix method to fit the measured ones, and dielectric functions of monolayer $MoSe_2$ can be obtained. Fig. 2(b) shows the optical models constructed for monolayer $MoSe_2$ samples on substrates of sapphire, silicon, and quartz, respectively. The samples are primarily described by an optical stack model composed of air, $MoSe_2$ layer, and substrate. Specifically, the optical model for the sample on the silicon substrate needs to consider the natural oxide layer that inevitably forms on the pure silicon substrate.

The thickness of the natural oxide layer, determined by SE, is 4.4 nm. This unusual thickness for natural oxide layer can be traced back to the substrate's prolonged exposure to air, combined with subsequent processing steps. Specifically, the sample underwent PMMA transfer, involving water contact and heating, and was later annealed at 200 °C. These factors likely contributed to the enhanced natural oxide layer thickness. According to other reports, the dielectric constants are approximately 11.5 for sapphire, 11.4 for silicon, 3.9 for silicon's natural oxide layer, and 3.76 for quartz, respectively[46–49]. Since the silicon substrate is composed of silicon and its natural oxide layer, its actual dielectric constant will be less than 11.4. As shown in Fig. 2(b), as dielectric constant of the substrate decreases, the dielectric screening effect experienced by the surface monolayer $MoSe_2$ gradually reduces, the distance between electron-hole pairs decreases, the Coulomb interaction increases, and the exciton binding energy increases. In this process, the optical properties of monolayer $MoSe_2$ also undergo slight changes, which can be intuitively demonstrated by the ellipsometric analysis. In addition to the optical model, the dielectric function of monolayer $MoSe_2$ on substrates of sapphire and quartz over the concerned energy range is parameterized by combining two Lorentz oscillators, one Gaussian oscillator, and four Tauc-Lorentz oscillators. The detailed reasons for choosing these oscillators have been placed in the supplementary material. While the dielectric function model for monolayer $MoSe_2$ on the silicon substrate is slightly different, which reduce a Tauc-Lorentz oscillator compared with the oscillator models of the other two samples. The dielectric function model spectra, specifically constructed using the oscillators, are displayed in Supplementary Material Fig. S3 (a-c). The detailed parameters of the oscillators are listed in Supplementary Material Table S1. We postulate that the absence of this Tauc-Lorentz oscillator signal is attributed to its weakness, potentially stemming from the enhanced amplitude and expanded linewidth of the two adjacent Tauc-Lorentz absorption peaks from the sample on the silicon substrate, thereby masking this feeble Tauc-Lorentz signal. The thicknesses of monocrystal monolayer 2H-phase $MoSe_2$ on three different substrates determined by the SE are consistent with each other, all around 0.68 nm, which highly agrees with previous reports and the AFM result shown in Fig. 1(c)[44,50]. Specific experimental measurements and fitting results of the ellipsometric spectra for monolayer $MoSe_2$ on sapphire, silicon, and quartz substrates are presented in Supplementary Material Fig. S4 (a-c). The experiments, fitting results and dielectric functions of these substrates are also included in Supplementary Material Fig. S5 (a-c) and Fig. S6 (a-d).

Fig. 3(a, b) presents the complex refractive index $N = n - ik$ of monolayer 2H $MoSe_2$ samples on substrates of sapphire, quartz, and silicon at room temperature (approximately 293 K) within the energy range of 1.24–4.76 eV, determined by the SE measurements and analysis. Here, n and k denote the refractive index and the extinction coefficient, respectively. The optical properties of monolayer 2H $MoSe_2$ samples are notably influenced by substrates with different dielectric constants. The exact transition energy positions can be determined by the CP analysis, up to six CPs labeled A-F can be found for the monolayer 2H $MoSe_2$ over the concern energy range, and their positions have been indicated in the extinction coefficient spectra in Fig. 3(b). It should be noted that despite the presence of seven oscillators in the dielectric model, only six CPs can be determined since the Gaussian oscillator does not have a direct physical significance. The monolayer 2H $MoSe_2$ on silicon substrate loses CP D, which is submerged by the increased amplitudes and broadening of CPs C and E. Furthermore, the sample on

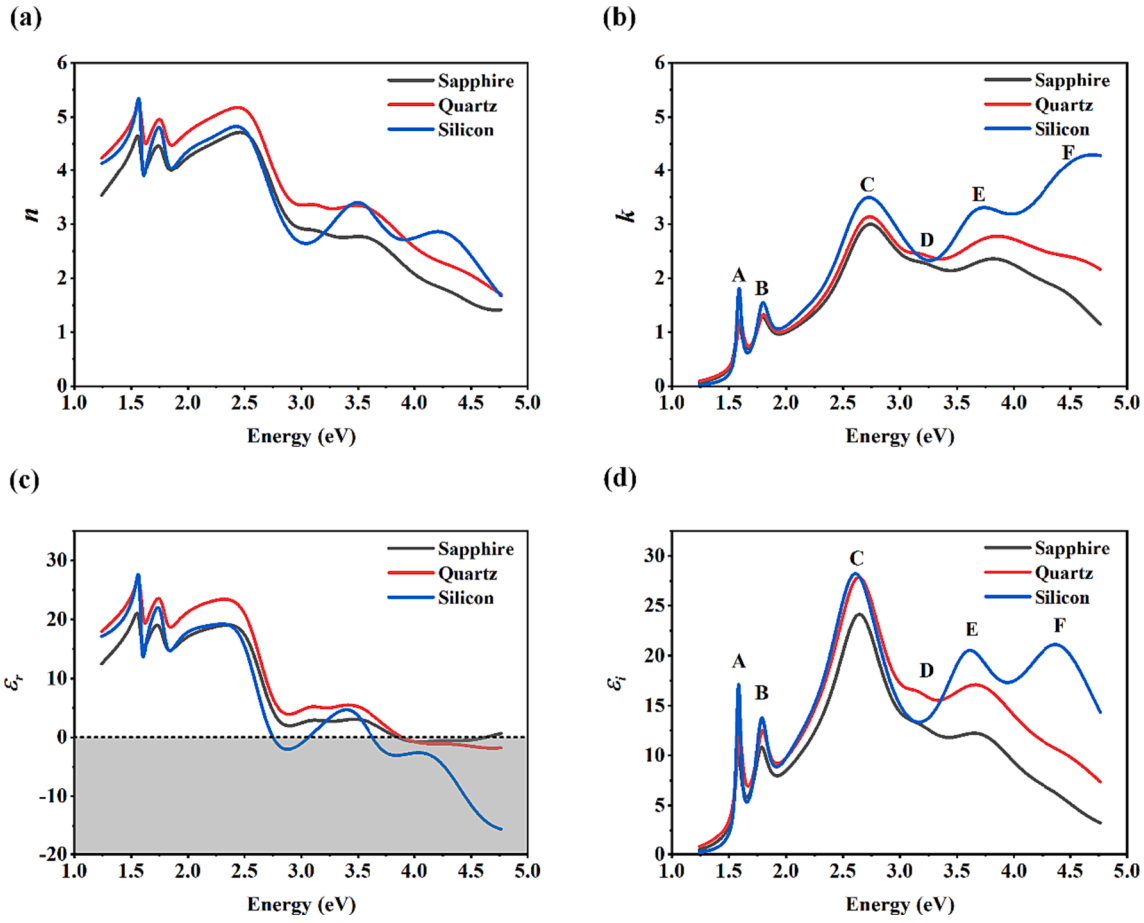

Fig. 3. (a,b) The refractive index n and extinction coefficient k of monolayer 2H $MoSe_2$ samples on sapphire, quartz, and silicon substrates; (c,d) The real component (ε_r) and imaginary element (ε_i) of the dielectric function for monolayer 2H $MoSe_2$ samples on sapphire, quartz, and silicon substrates.

silicon substrate displays more pronounced absorption peaks compared to those on the other two substrates, especially noticeable in the high-energy range. This phenomenon can be attributed to potential charge transfer between the substrate and the sample[51,52]. This transfer could cause electrons from the silicon substrate to migrate to the monolayer $MoSe_2$, thereby increasing the carrier concentration of the monolayer $MoSe_2$ and enhancing the light absorption in the high-energy region. This observation aligns with previous research finding[53].

Fig. 3(c, d) displays the dielectric function $\varepsilon = \varepsilon_r - i\varepsilon_i$ of monolayer 2H $MoSe_2$ samples on substrates of sapphire, quartz, and silicon over the concerned energy range of 1.24–4.76 eV, determined by SE measurements and analysis. Here, ε_r and ε_i are the real and imaginary parts of the dielectric function, and generally we have the relation $\varepsilon = N^2$ between the dielectric function and complex refractive index. The gray area in Fig. 3(c) represents negative ε_r regions, which is primarily caused by the surface plasmon resonance. This occurs because in $MoSe_2$, the five unoccupied d-orbitals are fully filled upon excitation by high-energy photons, thereby creating a small energy gap that separates these d-orbitals from the s and p orbitals, which dominate under high-energy conditions. This separation leads to the formation of surface plasmon resonances, manifesting as a negative ε_r region in the dielectric function [54]. Zero-crossing points can be determined by intersections between the ε_r curves of the samples on three different substrates and the zero-point dashed line. The energy of the zero-crossing point (E_{zc}) indicates the surface plasmon resonance frequency, and differences in E_{zc} are related to different substrate refractive indices, with 3.42, 1.76, and 1.46 for silicon, sapphire and quartz, respectively. The E_{zc} points of these three different substrate samples experience a redshift as the substrate refractive index increases, indicating that the surface plasmon frequency shifts toward lower energies, and the surface plasmon resonance region becomes broader. This is because the optical coupling between the 2D material and the substrate increases with the substrate refractive index, and the stronger optical coupling further result in a broader surface plasmon resonance of the monolayer $MoSe_2$ on substrate with a higher refractive index. This information is valuable for the design of plasmonic devices based on $MoSe_2$. Fig. 3(d) shows the spectra of the imaginary dielectric function ε_i of monolayer 2H $MoSe_2$ samples on the three different substrates. It can be observed that different substrates cause certain adjustments to the central energies, broadening, and amplitudes of the CP peaks (A-F). Moreover, it is obvious that the change in substrate does not significantly affect the intensity of the $MoSe_2$ dielectric function, and the high-energy absorption region becomes stronger on the silicon substrate, which is also consistent with previous research [53].

It is difficult for us to intuitively summarize the regulatory rules of the dielectric constant of the substrate on the optical properties of monolayer 2H $MoSe_2$ solely relying on dielectric function or extinction coefficient spectra. The CP analysis method is an efficient way to accurately determine the center energy and characteristics of these CP peaks and further quantitatively analyze the regulatory mechanism of the substrate effect on the optical properties of monolayer 2H $MoSe_2$[33,55]. CP analysis is achieved by fitting a series of parameters to the second derivative of the SE determined dielectric function with respect to the energy, as described by

$$\frac{d^2\varepsilon}{dE^2} = \begin{cases} m(m-1)Ae^{i\phi}(E - E_0 + i\Gamma)^{m-2}, & m \neq 0 \\ Ae^{i\phi}(E - E_0 + i\Gamma)^{-2}, & m = 0 \end{cases} \quad (2)$$

where, A, ϕ, E_0, and Γ respectively represent the amplitude, phase, center energy, and damping coefficient of the CP, and m is the spatial dimension of the wave vector with $m = 1/2$, 0, and $-1/2$ indicating that CP transition is 3-dimensional, 2-dimensional, and 1-dimensional, respectively [56]. Specially, $m = -1$ implies that the CP optical transition involve excitonic effect. When applying this method to monolayer 2H $MoSe_2$ samples, the best fitting results correspond to $m = -1$ for all six CPs, indicating that they are of excitonic-type transitions.

Fig. 4(a) displays the CP analysis results of monolayer $MoSe_2$ on three different substrates, comparatively giving the second derivative of the SE determined dielectric functions and the best fitting ones. For the silicon substrate, CP D is missing from the results, a phenomenon that is difficult to discern directly from the dielectric function spectra. The CP analysis results for these three samples align remarkably well with the experimental findings presented above but give more quantitative details, establishing a foundation for a precise analysis of the influence of substrate effects on the optical properties of monolayer $MoSe_2$. Fig. 4(b) reveals that as the dielectric constant of the substrate increases, the center energies of CPs A, B, and F decrease, indicating that the corresponding absorption peaks undergo redshifts mainly due to the enhanced dielectric screening effect. For CP A, which determines the optical bandgap of monolayer $MoSe_2$, and CP B, which determines the band splitting magnitude of spin–orbit coupling (SOC) effect, when the substrate changes from quartz to sapphire, the corresponding transitions experience redshifts of up to 10.3 meV and 9.7 meV, respectively. This observation is consistent with previous reports[27,57]. Considering the potential influence of other factors on the experimental results, although factors like temperature, pressure, and strain do indeed impact optical properties, our experiments were conducted under ambient conditions. Hence, the effects of temperature and pressure can be deemed negligible within this study's scope. In terms of strain, the transfer process of $MoSe_2$ onto different substrates does introduce strain. However, prior researches have indicated that the strain introduced during substrate transfer using the PMMA method is typically minimal and often leads to a reduction in the bandgap of monolayer TMDCs[58,59]. To alleviate the potential effects of strain, we annealed the transferred samples at 200 °C for one hour. This step is vital for eliminating any residual strain within the samples. The results from Fig. 4(b) demonstrate that $MoSe_2$ on sapphire substrates exhibits the smallest bandgap due to the maximum dielectric screening effect. When transferred to substrates with diminished dielectric screening effects, the bandgap of $MoSe_2$ consistently increases. This trend aligns closely with the anticipated dielectric screening effects introduced by various substrates and appears to be insignificantly affected by the minimal strain introduced during the substrate transfer process. Thus, it can be affirmed that the dielectric screening effects introduced by different substrates are the primary reason for the reduction in the center energies of CPs. Fig. 4(c) depicts the evolutions in the center energies of CPs C, D, and E as the dielectric constant of the substrate increases. It can be observed that for the sample on the silicon substrate, the only semiconductor among the three ones, CP D is absent, and the central energies of CPs C and E show noticeable redshifts compared to results for the other two substrates, maybe due to the electron transfer from the silicon substrate to the monolayer $MoSe_2$, which in turn alters the band structure[51]. For the results obtained from quartz and sapphire substrates, the center energies of CPs C, D, and E increase with the dielectric constant of the substrate. This suggests that these absorption peaks might undergo blueshifts due to the enhanced dielectric screening effect. It is should be noted that although CP C on quartz and sapphire substrates is very close to each other, the central energy is still slightly higher on the sapphire substrate as indicated by dashed lines in the Fig. 4(c). The detailed fitting parameters of CPs A–F are listed in Supplementary Material Table S2.

Fig. 4(d) illustrates a schematic diagram of the variation in the band structure of monolayer $MoSe_2$ as the substrate dielectric constant increases. It displays that the quasiparticle bandgap E_g of monolayer $MoSe_2$ is composed of the exciton binding energy E_b and the optical bandgap E_o, and the dielectric screening effect directly changes the quasiparticle bandgap E_g and exciton binding energy E_b. Specifically, the quasiparticle bandgap E_g decreases as the substrate dielectric constant increases primarily due to the image charge effect[27,60]. The decrease in exciton binding energy E_b is due to the weakened Coulomb interaction between electrons and holes caused by the increased substrate dielectric constant. Importantly, the decrease magnitudes in these two factors may differ from each other, which thereby leads to a shift in the optical

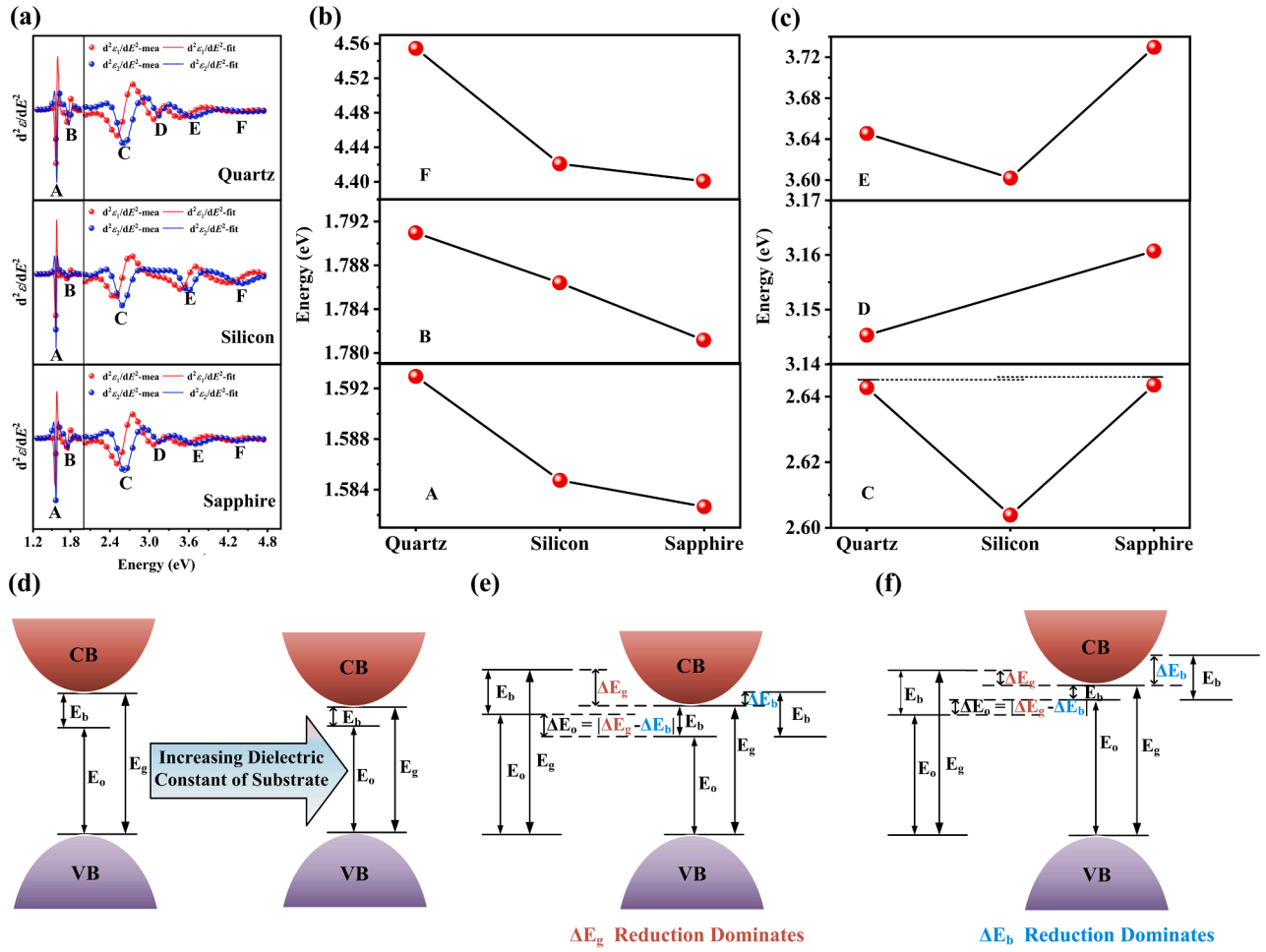

Fig. 4. (a) CP analysis results of the second derivative of the dielectric functions of monolayer $MoSe_2$ on substrates of quartz, silicon, and sapphire; (b) Evolutions of the center energies of CPs A, B, and F versus the substrate with the dielectric constant increasing; (c) Evolutions of the center energies of CPs C, D, and E versus the substrate with the dielectric constant increasing; (d) Schematic diagram showing the changes in the band structure of monolayer $MoSe_2$ with the substrate dielectric constant increasing; (e) and (f) Schematic diagrams of the optical bandgap variations of monolayer $MoSe_2$ dominated by reductions in the quasiparticle bandgap and in the exciton binding energy, respectively.

bandgap. Fig. 4(e) and 4(f) further schematically illustrate the variations in the optical bandgap of monolayer $MoSe_2$ dominated by different factors. The change in the optical bandgap equals to the absolute difference between the decreases in the quasiparticle bandgap and exciton binding energy, i.e., $\Delta E_o = |\Delta E_g - \Delta E_b|$. When the decrease in the quasiparticle bandgap is greater than that in the exciton binding energy, the optical bandgap undergoes a redshift as shown in Fig. 4(e), and vice versa as shown in Fig. 4(f). Therefore, it can be concluded that the redshifts in CPs A, B, and F are because the decrease in the quasiparticle bandgap is greater than that in the exciton binding energy, while the situation for CPs C, D, and E is exactly the opposite.

Finally, to further ascertain the details of the optical transitions corresponding to the six CPs of monolayer $MoSe_2$, first-principles calculations are introduced to establish connections between the SE determined CPs and the band structure through isoenergetic and isomomentum lines. Fig. 5(a) illustrates the calculated band structure of the monolayer $MoSe_2$ within the projected Brillouin zone relevant k-branches based on the PBE approximation considering the SOC effects. It should be noted that although the PBE bandgap is lower than the experimental optical bandgap, the band dispersion structure is relatively accurate[61]. The monolayer $MoSe_2$ has been confirmed to have a direct optical bandgap and the corresponding transition occur at the smallest bandgap at the K symmetry point in the Brillouin zone. The first-principle calculated bandgap is artificially widened to match the experimental optical bandgap 1.593 eV, which thereby helps to better determine the locations of the CP optical transitions[20,50]. Fig. 5(b) displays the partial density of states (PDOS) of monolayer $MoSe_2$, indicating that the CP optical transitions in monolayer $MoSe_2$ are mainly contributed by the electrons in the 4d orbitals of Mo atom and the 4p orbitals of Se atom. Fig. 5(c) shows the energy difference curves ($E_c - E_v$) between the conduction and valence bands involved in these CP optical transitions. Here, V_i and C_i respectively represent the i-th highest valence band and the i-th lowest conduction band, while V_i' and C_i' represent the lower and higher bands split from V_i and C_i considering the SOC effect. Fig. 5(d) shows the CP analysis results of monolayer $MoSe_2$. Here, the sample on the quartz substrate is taken as an example to analyze the details of the CP optical transitions, since the quartz has the smallest dielectric constant, which has the weakest dielectric screening effect and closest to the condition of first-principles calculations.

According to the microscopic theory of dielectric functions[62], the JDOS determines the optical transition probability, which can be represented as

$$JDOS = \frac{1}{4\pi^3}\int \frac{dS}{|\nabla_K(E_C - E_V)|}, \tag{3}$$

where S represents the constant energy surface defined by $E_c - E_v = E_i$, and E_i represents the energy of the incident photon[63]. When the gradient $\nabla_k(E_c - E_v)$ in k-space tends to zero, the JDOS is singular, corresponding to the van Hove singularity, which can be considered to

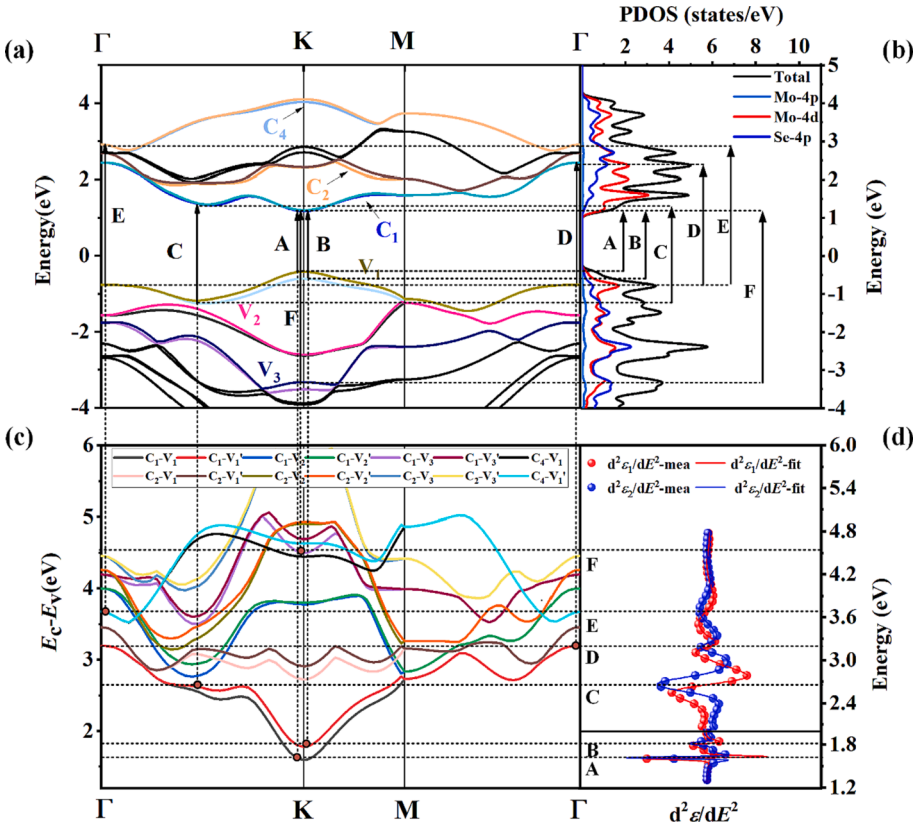

Fig. 5. (a) The band structure of monolayer 2H $MoSe_2$ on the relevant k-branches within the projected Brillouin zone; (b) The PDOS of monolayer 2H $MoSe_2$ within the corresponding energy range; (c) Energy difference curves between the valence and conduction bands; (d) The second derivative of the SE determined dielectric functions of monolayer 2H $MoSe_2$ and best fitting ones by the CP analysis method. Here, capital letters A-F represent the six CP optical transitions, the connected dashed lines are isoenergetic lines and isomomentum lines, red dots in Fig. 5(c) are the tangent points, and black solid arrows in Fig. 5(a) represent the CP optical transitions from valence bands to conduction bands. (For interpretation of the references to colour in this figure legend, the reader is referred to the web version of this article.)

be the physical origin of the CPs in the dielectric function[31,33,64]. Based on this point, isoenergetic lines are drawn over the center energies of CPs in Fig. 5(d), and the tangent points on the band energy difference curves represented by red dots in Fig. 5(c) indicate the gradient $\nabla_k(E_c - E_v) = 0$ and thereby can be used to determine the positions of CP optical transitions in the momentum space[64]. Further isomomentum lines are drawn from these tangent points to connect the interband transitions between the corresponding valence and conduction bands in Fig. 5(a), which can determine the specific transition positions of the CPs in the band structure. Finally, isoenergetic lines are drawn once again from the transition start and end positions in band structure to the PDOS in Fig. 5 (b), to determine the electrons from specific elements and orbitals involved in each CP optical transition.

From Fig. 5(a), It is observable that CPs A and B correspond to the well-reported interband direct transitions respectively from V_1 and V_1' to C_1 at the K symmetry point (1.593 eV, 1.791 eV). The band splitting value due the SOC effect is determined to be 198 meV, highly agrees with previous results[20,65]. CP C corresponds to the multiple interband transitions from V_1' to C_1 between the proximity of the Γ and K symmetry points (2.641 eV). CPs D and E correspond to the multiple interband transitions respectively from V_1 to C_1 and C_2 around the Γ symmetry point (3.141 eV, 3.659 eV). While CP F is attributed to the multiple interband transitions from V_3 to C_1 around the K symmetry point (4.584 eV). From Fig. 5(b), it further confirms that these CP transitions are mainly contributed by the electrons from Mo's 4d orbitals and Se's 4p orbitals. Combined with the results of Fig. 4(b, c), it becomes evident that with the increase of the substrate dielectric constant, thereby enhancing the dielectric screening effect of monolayer $MoSe_2$, the optical transitions occurring at the K point in momentum space will undergo redshifts due to the decrease of the quasiparticle bandgap ΔE_g greater than the decrease of the exciton binding energy ΔE_b. However, optical transitions occurring outside the K point in momentum space will undergo blueshifts due to the decrease of the quasiparticle bandgap ΔE_g being less than the decrease of the exciton binding energy ΔE_b. Therefore, our investigations underscore that the quasiparticle bandgap E_g associated with electronic transitions at the K-point is particularly sensitive to variations in the surrounding dielectric environment. This sensitivity manifests as a distinct redshift in these transitions with an increment in the substrate's dielectric constant. However, for electronic transitions away from the K-point, specifically involving excitons C, D, and E, the behavior is less straightforward. On transparent insulating substrates like sapphire and quartz, the exciton binding energy E_b of monolayer $MoSe_2$ appears to be more sensitive to changes in the dielectric environment, leading to blueshifts. Notably, the near-identical positions of peak C on quartz and sapphire substrates could indeed represent the same point, suggesting that for transitions between high-symmetry points Γ and K, the exciton binding energy E_b and the quasiparticle bandgap E_g may have similar sensitivities to changes in the dielectric environment. On the silicon substrate, the situation becomes more intricate. Potential electron transfer between the substrate and $MoSe_2$ could alter the band structure, thereby affecting the excitonic features. We hypothesize that the absence of the D peak and the redshift of peaks C and E on the silicon substrate could be due to a combination of electron transfer from the silicon substrate to $MoSe_2$ and an enhanced sensitivity of the quasiparticle bandgap E_g to changes in the dielectric environment. The observed phenomena suggest that a judicious selection of substrate material can be a pivotal tool for modulating specific electronic transitions, offering a robust foundation for the design of

optoelectronic devices based on two-dimensional semiconductors such as $MoSe_2$. The intricate mechanisms underlying these observations warrant further exploration in future studies.

4. Conclusion

In conclusion, this study offers a comprehensive analysis of the influence exerted by the substrate dielectric constant on the optical properties of monolayer $MoSe_2$. Precise extraction of the dielectric functions of monolayer $MoSe_2$ on various substrates is achieved through spectroscopic ellipsometry, revealing a range from 1.24 to 4.76 eV. By meticulously comparing and analyzing the fitting results of the second derivative of the dielectric function's CPs, we demonstrate that alterations in substrate type (quartz, silicon, sapphire) can impact the optical properties of monolayer $MoSe_2$, prompting notable shifts in absorption peaks due to differential dielectric screening effects. The most prominently observed absorption peaks, A and B, exhibit red shifts up to 10.3 meV and 9.7 meV, respectively. Our findings indicate that the positions of CPs corresponding to optical transitions in the $MoSe_2$ layer can undergo redshifts or blueshifts, contingent upon the relative changes in the quasi-particle bandgap and exciton binding energy incited by variations in the substrate dielectric constant. Additionally, a potential electron transfer from the silicon substrate to the monolayer $MoSe_2$ is discerned, possibly accounting for changes in its band structure. By integrating CP analysis with first-principles calculations, we further elucidate the details of optical transitions corresponding to six CPs (A-F) in monolayer $MoSe_2$ on various substrates. This method, which takes into account isoenergetic and isomomentum lines, affords a more precise understanding of these transitions and the electronic states contributing to them. By employing this methodology, we have ascertained that transitions at the momentum space K-point (CPs A, B and F) undergo redshifts with increasing substrate dielectric constant. Conversely, transitions outside the K-point (CPs C, D, and E) predominantly blueshift on transparent insulating substrates like sapphire and quartz. Yet, the behavior on the silicon substrate deviates, with potential electron transfer and an augmented sensitivity of the quasiparticle bandgap E_g playing pivotal roles. Notably, the near-identical positions of peak C on quartz and sapphire substrates hint at a comparable sensitivity of the exciton binding energy E_b and the quasiparticle bandgap E_g to dielectric changes between high-symmetry points Γ and K. Our research underscores the importance of substrate selection in the design of $MoSe_2$-based optoelectronic devices, offering valuable insights into tailoring the optical properties of two-dimensional materials through substrate engineering. This knowledge is of paramount importance for the further study and potential applications of $MoSe_2$ and other similar two-dimensional materials.

CRediT authorship contribution statement

Liusheng Huang: Conceptualization, Formal analysis, Investigation, Visualization, Writing – original draft, Writing – review & editing. **Honggang Gu:** Conceptualization, Methodology, Supervision, Writing – review & editing. **Mingsheng Fang:** Investigation. **Shiyuan Liu:** Supervision, Project administration, Funding acquisition, Writing – review & editing.

Declaration of Competing Interest

The authors declare that they have no known competing financial interests or personal relationships that could have appeared to influence the work reported in this paper.

Data availability

Data will be made available on request.

Acknowledgments

This work was funded by the National Key Research and Development Plan of China (Grant No. 2022YFB2803900), National Natural Science Foundation of China (Grant No. 52130504), Guangdong Basic and Applied Basic Research Foundation (Grant No. 2023A1515030149), Key Research and Development Program of Hubei Province (Grant No. 2021BAA013), Natural Science Foundation of Hubei Province (Grant No. 2021CFB322), the Innovation Project of Optics Valley Laboratory (Grant No. OVL2023PY003), and the Fundamental Research Funds for the Central Universities (Grant No. 2021XXJS113). The authors thank the technical support from the Experiment Centre for Advanced Manufacturing and Technology in School of Mechanical Science &Engineering of HUST.

Appendix A. Supplementary data

Supplementary data to this article can be found online at https://doi.org/10.1016/j.apsusc.2023.158748.

References

[1] D. Akinwande, C. Huyghebaert, C.-H. Wang, M.I. Serna, S. Goossens, L.-J. Li, H.-S.-P. Wong, F.H. Koppens, Graphene and two-dimensional materials for silicon technology, Nature 573 (2019) 507–518.
[2] G. Fiori, F. Bonaccorso, G. Iannaccone, T. Palacios, D. Neumaier, A. Seabaugh, S. K. Banerjee, L. Colombo, Electronics based on two-dimensional materials, Nat. Nanotechnol. 9 (2014) 768–779.
[3] Y. Liu, Y. Huang, X. Duan, Van der Waals integration before and beyond two-dimensional materials, Nature 567 (2019) 323–333.
[4] S. Chen, G. Shi, Two-dimensional materials for halide perovskite-based optoelectronic devices, Adv. Mater. 29 (2017) 1605448.
[5] H.-P. Komsa, A.V. Krasheninnikov, Effects of confinement and environment on the electronic structure and exciton binding energy of MoS 2 from first principles, Phys. Rev. B 86 (2012), 241201.
[6] S. Kim, A. Konar, W.-S. Hwang, J.H. Lee, J. Lee, J. Yang, C. Jung, H. Kim, J.-B. Yoo, J.-Y. Choi, High-mobility and low-power thin-film transistors based on multilayer MoS2 crystals, Nat. Commun. 3 (2012) 1011.
[7] G. Ermolaev, D. Grudinin, Y. Stebunov, K.V. Voronin, V. Kravets, J. Duan, A. Mazitov, G. Tselikov, A. Bylinkin, D. Yakubovsky, Giant optical anisotropy in transition metal dichalcogenides for next-generation photonics, Nat. Commun. 12 (2021) 854.
[8] C.-Z. Ning, L. Dou, P. Yang, Bandgap engineering in semiconductor alloy nanomaterials with widely tunable compositions, Nat. Rev. Mater. 2 (2017) 1–14.
[9] M. Onga, Y. Zhang, T. Ideue, Y. Iwasa, Exciton Hall effect in monolayer MoS2, Nat. Mater. 16 (2017) 1193–1197.
[10] N. Saigal, V. Sugunakar, S. Ghosh, Exciton binding energy in bulk MoS2: A reassessment, Appl. Phys. Lett. 108 (2016), 132105.
[11] A. Splendiani, L. Sun, Y. Zhang, T. Li, J. Kim, C.-Y. Chim, G. Galli, F. Wang, Emerging photoluminescence in monolayer MoS2, Nano Lett. 10 (2010) 1271–1275.
[12] G. Eda, H. Yamaguchi, D. Voiry, T. Fujita, M. Chen, M. Chhowalla, Photoluminescence from chemically exfoliated MoS2, Nano Lett. 11 (2011) 5111–5116.
[13] I. Kylänpää, H.-P. Komsa, Binding energies of exciton complexes in transition metal dichalcogenide monolayers and effect of dielectric environment, Phys. Rev. B 92 (2015), 205418.
[14] T. Cheiwchanchamnangij, W.R. Lambrecht, Quasiparticle band structure calculation of monolayer, bilayer, and bulk MoS 2, Phys. Rev. B 85 (2012), 205302.
[15] K. Hao, J.F. Specht, P. Nagler, L. Xu, K. Tran, A. Singh, C.K. Dass, C. Schüller, T. Korn, M. Richter, Neutral and charged inter-valley biexcitons in monolayer MoSe2, Nat. Commun. 8 (2017) 15552.
[16] H. Xie, S. Jiang, D.A. Rhodes, J.C. Hone, J. Shan, K.F. Mak, Tunable exciton-optomechanical coupling in suspended monolayer MoSe2, Nano Lett. 21 (2021) 2538–2543.
[17] T. Chowdhury, K. Jo, S.B. Anantharaman, T.H. Brintlinger, D. Jariwala, T. J. Kempa, Anomalous room-temperature photoluminescence from nanostrained MoSe2 monolayers, ACS Photonics 8 (2021) 2220–2226.
[18] H. Liu, L. Jiao, F. Yang, Y. Cai, X. Wu, W. Ho, C. Gao, J. Jia, N. Wang, H. Fan, Dense network of one-dimensional midgap metallic modes in monolayer MoSe 2 and their spatial undulations, Phys. Rev. Lett. 113 (2014), 066105.
[19] Y. Yu, G.-H. Nam, Q. He, X.-J. Wu, K. Zhang, Z. Yang, J. Chen, Q. Ma, M. Zhao, Z. Liu, High phase-purity 1T′-MoS2-and 1T′-MoSe2-layered crystals, Nat. Chem. 10 (2018) 638–643.
[20] Y. Zhang, T.-R. Chang, B. Zhou, Y.-T. Cui, H. Yan, Z. Liu, F. Schmitt, J. Lee, R. Moore, Y. Chen, Direct observation of the transition from indirect to direct bandgap in atomically thin epitaxial MoSe2, Nat. Nanotechnol. 9 (2014) 111–115.

[21] J.C. Shaw, H. Zhou, Y. Chen, N.O. Weiss, Y. Liu, Y. Huang, X. Duan, Chemical vapor deposition growth of monolayer MoSe 2 nanosheets, Nano Res. 7 (2014) 511–517.
[22] X. Wang, Y. Gong, G. Shi, W.L. Chow, K. Keyshar, G. Ye, R. Vajtai, J. Lou, Z. Liu, E. Ringe, Chemical vapor deposition growth of crystalline monolayer MoSe2, ACS Nano 8 (2014) 5125–5131.
[23] C. Li, Q. Wang, H. Diao, Z. Hao, W. Yu, K. Liu, X. Gan, F. Xiao, J. Zhao, Enhanced photoluminescence of monolayer MoSe2 in a double resonant plasmonic nanocavity with fano resonance and mode matching, Laser Photonics Rev. 16 (2022) 2100199.
[24] X. Fu, F. Li, J.-F. Lin, Y. Gong, X. Huang, Y. Huang, B. Han, Q. Zhou, T. Cui, Pressure-dependent light emission of charged and neutral excitons in monolayer MoSe2, J. Phys. Chem. Lett. 8 (2017) 3556–3563.
[25] M.M. Ugeda, A.J. Bradley, S.-F. Shi, F.H. Da Jornada, Y. Zhang, D.Y. Qiu, W. Ruan, S.-K. Mo, Z. Hussain, Z.-X. Shen, Giant bandgap renormalization and excitonic effects in a monolayer transition metal dichalcogenide semiconductor, Nat. Mater. 13 (2014) 1091–1095.
[26] D.Y. Qiu, F.H. da Jornada, S.G. Louie, Environmental screening effects in 2D materials: renormalization of the bandgap, electronic structure, and optical spectra of few-layer black phosphorus, Nano Lett. 17 (2017) 4706–4712.
[27] M. Drüppel, T. Deilmann, P. Krüger, M. Rohlfing, Diversity of trion states and substrate effects in the optical properties of an MoS2 monolayer, Nat. Commun. 8 (2017) 2117.
[28] S. Borghardt, J.-S. Tu, F. Winkler, J. Schubert, W. Zander, K. Leosson, B. E. Kardynał, Engineering of optical and electronic band gaps in transition metal dichalcogenide monolayers through external dielectric screening, Phys. Rev. Mater. 1 (2017), 054001.
[29] Y. Kajino, K. Oto, Y. Yamada, Modification of optical properties in monolayer WS2 on dielectric substrates by coulomb engineering, J. Phys. Chem. C 123 (2019) 14097–14102.
[30] W. Shen, Y. Wei, C. Hu, C. López-Posadas, M. Hohage, L. Sun, Substrate induced optical anisotropy in monolayer MoS2, J. Phys. Chem. C 124 (2020) 15468–15473.
[31] M. Fang, Z. Wang, H. Gu, M. Tong, B. Song, X. Xie, T. Zhou, X. Chen, H. Jiang, T. Jiang, Layer-dependent dielectric permittivity of topological insulator Bi2Se3 thin films, Appl. Surf. Sci. 509 (2020), 144822.
[32] H. Gu, B. Song, M. Fang, Y. Hong, X. Chen, H. Jiang, W. Ren, S. Liu, Layer-dependent dielectric and optical properties of centimeter-scale 2D WSe 2: evolution from a single layer to few layers, Nanoscale 11 (2019) 22762–22771.
[33] B. Song, H. Gu, M. Fang, X. Chen, H. Jiang, R. Wang, T. Zhai, Y.T. Ho, S. Liu, Layer-dependent dielectric function of wafer-scale 2D MoS2, Adv. Opt. Mater. 7 (2019) 1801250.
[34] Y. Li, A. Chernikov, X. Zhang, A. Rigosi, H.M. Hill, A.M. Van Der Zande, D. A. Chenet, E.-M. Shih, J. Hone, T.F. Heinz, Measurement of the optical dielectric function of monolayer transition-metal dichalcogenides: MoS 2, Mo S e 2, WS 2, and WS e 2, Phys. Rev. B 90 (2014), 205422.
[35] H.G. Park, T.J. Kim, F. Ullah, V.L. Le, H.T. Nguyen, Y.S. Kim, Y.D. Kim, Temperature dependence of the dielectric function of monolayer MoSe2, Sci. Rep. 8 (2018) 3173.
[36] P.B. James, M. Lavik, The crystal structure of MoSe2, Acta Crystallogr. 16 (1963) 1183.
[37] J. Hafner, Ab-initio simulations of materials using VASP: Density-functional theory and beyond, J. Comput. Chem. 29 (2008) 2044–2078.
[38] S. Grimme, Semiempirical GGA-type density functional constructed with a long-range dispersion correction, J. Comput. Chem. 27 (2006) 1787–1799.
[39] S. Tongay, J. Zhou, C. Ataca, K. Lo, T.S. Matthews, J. Li, J.C. Grossman, J. Wu, Thermally driven crossover from indirect toward direct bandgap in 2D semiconductors: MoSe2 versus MoS2, Nano Lett. 12 (2012) 5576–5580.
[40] X. Lu, M.I.B. Utama, J. Lin, X. Gong, J. Zhang, Y. Zhao, S.T. Pantelides, J. Wang, Z. Dong, Z. Liu, Large-area synthesis of monolayer and few-layer MoSe2 films on SiO2 substrates, Nano Lett. 14 (2014) 2419–2425.
[41] B. Zheng, Y. Chen, Controllable growth of monolayer MoS2 and MoSe2 crystals using three-temperature-zone furnace, in: IOP conference series: materials science and engineering, IOP Publishing, 2017, p. 012085.
[42] D. Li, C. Trovatello, S. Dal Conte, M. Nuß, G. Soavi, G. Wang, A.C. Ferrari, G. Cerullo, T. Brixner, Exciton–phonon coupling strength in single-layer MoSe2 at room temperature, Nat. Commun. 12 (2021) 954.
[43] J. Mann, Q. Ma, P.M. Odenthal, M. Isarraraz, D. Le, E. Preciado, D. Barroso, K. Yamaguchi, G. von Son Palacio, A. Nguyen, 2-Dimensional transition metal dichalcogenides with tunable direct band gaps: MoS2 (1–x) Se2x monolayers, Adv. Mater. 26 (2014) 1399–1404.
[44] Y.-H. Chang, W. Zhang, Y. Zhu, Y. Han, J. Pu, J.-K. Chang, W.-T. Hsu, J.-K. Huang, C.-L. Hsu, M.-H. Chiu, Monolayer MoSe2 grown by chemical vapor deposition for fast photodetection, ACS Nano 8 (2014) 8582–8590.
[45] H. Gu, X. Chen, H. Jiang, C. Zhang, S. Liu, Optimal broadband Mueller matrix ellipsometer using multi-waveplates with flexibly oriented axes, J. Opt. 18 (2016), 025702.
[46] S. Park, N. Mutz, T. Schultz, S. Blumstengel, A. Han, A. Aljarb, L.-J. Li, E.J. List-Kratochvil, P. Amsalem, N. Koch, Direct determination of monolayer MoS 2 and WSe 2 exciton binding energies on insulating and metallic substrates, 2D Materials 5 (2018), 025003.
[47] J. Robertson, High dielectric constant oxides, Eur. Phys. J.-Appl. Phys. 28 (2004) 265–291.
[48] S. Baroni, R. Resta, Ab initio calculation of the macroscopic dielectric constant in silicon, Phys. Rev. B 33 (1986) 7017.
[49] P. Sarafis, A.G. Nassiopoulou, Dielectric properties of porous silicon for use as a substrate for the on-chip integration of millimeter-wave devices in the frequency range 140 to 210 GHz, Nanoscale Res. Lett. 9 (2014) 1–8.
[50] J. Xia, X. Huang, L.-Z. Liu, M. Wang, L. Wang, B. Huang, D.-D. Zhu, J.-J. Li, C.-Z. Gu, X.-M. Meng, CVD synthesis of large-area, highly crystalline MoSe 2 atomic layers on diverse substrates and application to photodetectors, Nanoscale 6 (2014) 8949–8955.
[51] J.P.B. Silva, C. Almeida Marques, A. Viana, L. Santos, K. Gwozdz, E. Popko, J. Connolly, K. Veltruská, V. Matolín, O. Conde, Morphological, optical and photovoltaic characteristics of MoSe2/SiOx/Si heterojunctions, Sci. Rep. 10 (2020) 1215.
[52] M.K. Man, S. Deckoff-Jones, A. Winchester, G. Shi, G. Gupta, A.D. Mohite, S. Kar, E. Kioupakis, S. Talapatra, K.M. Dani, Protecting the properties of monolayer MoS2 on silicon based substrates with an atomically thin buffer, Sci. Rep. 6 (2016) 20890.
[53] G.A. Ermolaev, Y.V. Stebunov, A.A. Vyshnevyy, D.E. Tatarkin, D.I. Yakubovsky, S. M. Novikov, D.G. Baranov, T. Shegai, A.Y. Nikitin, A.V. Arsenin, Broadband optical properties of monolayer and bulk MoS2, npj 2D, Mater. Appl. 4 (2020) 21.
[54] A. Beal, H. Hughes, Kramers-Kronig analysis of the reflectivity spectra of 2H-MoS2, 2H-MoSe2 and 2H-MoTe2, J. Phys. C Solid State Phys. 12 (1979) 881.
[55] M. Medikonda, G.R. Muthinti, R. Vasić, T.N. Adam, A. Reznicek, M. Wormington, G. Malladi, Y. Kim, Y.-C. Huang, A.C. Diebold, Optical properties of pseudomorphic Ge1− xSnx (x= 0 to 0.11) alloys on Ge (001), J. Vac. Sci. Technol. B 32 (2014).
[56] H. Fujiwara, R.W. Collins, Spectroscopic Ellipsometry for Photovoltaics, Springer, 2018.
[57] S. Lippert, L.M. Schneider, D. Renaud, K.N. Kang, O. Ajayi, J. Kuhnert, M.-U. Halbich, O.M. Abdulmunem, X. Lin, K. Hassoon, Influence of the substrate material on the optical properties of tungsten diselenide monolayers, 2D Mater. 4 (2017), 025045.
[58] E.M. Alexeev, N. Mullin, P. Ares, H. Nevison-Andrews, O. Skrypka, T. Godde, A. Kozikov, L. Hague, Y. Wang, K.S. Novoselov, Emergence of highly linearly polarized interlayer exciton emission in MoSe2/WSe2 heterobilayers with transfer-induced layer corrugation, ACS Nano 14 (2020) 11110–11119.
[59] C. Ernandes, L. Khalil, H. Henck, M.-Q. Zhao, J. Chaste, F. Oehler, A.T.C. Johnson, M.C. Asensio, D. Pierucci, M. Pala, Strain and spin-orbit coupling engineering in twisted WS2/graphene heterobilayer, Nanomaterials 11 (2021) 2921.
[60] K. Tanaka, T. Takahashi, T. Kondo, T. Umebayashi, K. Asai, K. Ema, Image charge effect on two-dimensional excitons in an inorganic-organic quantum-well crystal, Phys. Rev. B 71 (2005), 045312.
[61] P. Johari, V.B. Shenoy, Tuning the electronic properties of semiconducting transition metal dichalcogenides by applying mechanical strains, ACS Nano 6 (2012) 5449–5456.
[62] Y. Peter, M. Cardona, Fundamentals of semiconductors: physics and materials properties, Springer Science & Business Media, 2010.
[63] M. Cardona, Y.Y. Peter, Fundamentals of semiconductors, Springer, 2005.
[64] A.M. Leguy, P. Azarhoosh, M.I. Alonso, M. Campoy-Quiles, O.J. Weber, J. Yao, D. Bryant, M.T. Weller, J. Nelson, A. Walsh, Experimental and theoretical optical properties of methylammonium lead halide perovskites, Nanoscale 8 (2016) 6317–6327.
[65] J.S. Ross, S. Wu, H. Yu, N.J. Ghimire, A.M. Jones, G. Aivazian, J. Yan, D. G. Mandrus, D. Xiao, W. Yao, Electrical control of neutral and charged excitons in a monolayer semiconductor, Nat. Commun. 4 (2013) 1474.